Abel Santos, Taj Pereira, Cheryl Suwen Law and Dusan Losic
Rational engineering of nanoporous anodic alumina optical bandpass filters
Nanoscale, 2016; 8(31):14846-14857

Published at: http://dx.doi.org/10.1039/c6nr03490j

Nanoscale

RSCPublishing

PAPER

Rational Engineering of Nanoporous Anodic Alumina Optical Bandpass Filters

Cite this: DOI: 10.1039/xoxxoooooox

Abel Santos[1,2,3*], Taj Pereira[1], Cheryl Suwen Law[1] and Dusan Losic[1*]

Received ooth August 2016,
Accepted ooth August 2016

DOI: 10.1039/xoxxoooooox

www.rsc.org/

Herein, we present a rationally designed advanced nanofabrication approach aiming at producing a new type of optical bandpass filters based on nanoporous anodic alumina photonic crystals. The photonic stop band of nanoporous anodic alumina (NAA) is engineered in depth by means of a pseudo-stepwise pulse anodisation (PSPA) approach consisting in pseudo-stepwise asymmetric current density pulses. This nanofabrication method makes it possible to tune the transmission bands of NAA at specific wavelengths and bandwidths, which can be broadly modified across the UV-visible-NIR spectrum through the anodisation period (i.e. time between consecutive pulses). First, we establish the effect of the anodisation period as a means of tuning the position and width of the transmission bands of NAA across the UV-visible-NIR spectrum. To this end, a set of nanoporous anodic alumina bandpass filters (NAA-BPFs) are produced with different anodisation periods, ranging from 500 to 1200 s, and their optical properties (i.e. characteristic transmission bands and interferometric colours) are systematically assessed. Then, we demonstrate that the rational combination of stacked NAA-BPFs consisting of layers of NAA produced with different PSPA periods can be readily used to create a set of unique and highly selective optical bandpass filters with characteristic transmission bands, the position, width and number of which can be precisely engineered by this rational anodisation approach. Finally, as a proof-of-concept, we demonstrate that the superposition of stacked NAA-BPFs produced with slight modifications of the anodisation period enables the fabrication of NAA-BPFs with unprecedented broad transmission bands across the UV-visible-NIR spectrum. The results obtained from our study constitute the first comprehensive rationale towards advanced NAA-BPFs with fully controllable photonic properties. These photonic crystal structures could become a promising alternative to traditional optical bandpass filters based on glass and plastic.

Introduction

Optical bandpass filters (BPFs) are photonic structures that allow the transmission of a specific portion of the light spectrum in a selective manner while impeding the pass of light of all other wavelengths.[1] BPFs are extensively used across a broad range of disciplines and industries, including photography, astronomy, pharmaceutical industry, medicine, physics and chemistry. Generally, BPFs are classified into three categories according to the range of allowed wavelengths: namely; i) longpass filters, which allow the transmission of light of long wavelengths, ii) shortpass filters, which allow the pass of light of short wavelengths and iii) bandpass filters, which allow the transmission of a band of wavelengths while blocking the pass of light of shorter and longer wavelengths. However, other types of BPFs with complex transmission bands (i.e. several transmission bands located at different sections of the UV-visible-NIR spectrum) can be fabricated as well. Furthermore, the bandwidth and the blocking range of BPFs (i.e. the width of wavelengths that are allowed to pass and the wavelength interval that is attenuated by the filter, respectively) can be engineered to be narrow or wide. The cut-off between the maximum and minimum of transmission can also be designed to be gradual or sharp. Typically, BPFs are made from glass or plastic (e.g. polycarbonate or acrylic plastic), to which inorganic or organic compounds are incorporated during the fabrication process in order to impede the transmission of light of specific wavelengths.[2] In the last decades, the rise of nanotechnology has boosted a plethora of possibilities to engineer photonic structures with unique optical properties. In particular, nanoporous materials produced by electrochemical oxidation (i.e. anodisation) have been demonstrated as outstanding alternative platforms to produce numerous photonic structures for a broad range of applications.[3-6] Among these materials, nanoporous anodic alumina (NAA) produced by anodisation of aluminium substrates has long been envisaged as a platform to develop photonic crystal structures.[7-13] This nanoporous material can be produced by a cost-competitive and industrially scalable process, traditionally used by metal finishing industry.[14-16] Moreover, NAA is biocompatible and has good mechanical strength, thermal stability, chemical resistance and its nanopores feature a highly controllable and versatile cylindrical geometry.[3,4] In spite of these advantages, the generation of NAA-based photonic structures with precisely engineered optical properties has remained challenging due to the intrinsic limitations of this nanomaterial (i.e. low refractive index – $n_{Alumina}$ = 1.77 and low level of porosity).[3] In addition, anodisation of aluminium is an electrochemical process that relies on the diffusion of ionic species (e.g. Al^{3+}, O^{2-}, OH^-, etc.)

from and to the bulk electrolyte and across the oxide barrier layer located at the bottom tip of the nanopores, which insulates the inner side of the nanopores from the aluminium substrate.[17-21] Pioneering studies demonstrated that pulse-like anodisation approaches performed under specific conditions can make it possible to engineer the effective medium of NAA in depth with precision.[22-28] Recently, some of these approaches have been used to produce numerous NAA-based photonic structures, including rugate filters, optical microcavities, Fabry-Perót interferometers and distributed Bragg reflectors.[29-39] The development of optical platforms based on NAA has spread the use of this nanomaterial, typically used as a nanoporous template to grow other nanostructures such as nanowires and nanotubes[15], towards more relevant applications such as optical sensing systems, drug delivery chips and photonic tags.[40-51]

In this study, we present an innovative and rationally designed pulse anodisation approach, so called pseudo-stepwise pulse anodisation (PSPA), which enables the fabrication of nanoporous anodic alumina optical bandpass filters (NAA-BPFs) with advanced optical properties (**Fig. 1**). This nanofabrication approach makes it possible to engineer the photonic stop band of NAA in depth with precision by means of pseudo-stepwise current density pulses. First, we demonstrate that the transmission band of NAA-BPFs can be precisely positioned across the UV-visible-NIR spectrum by modifying the anodisation period (i.e. time between consecutive anodisation pulses). This rationale is subsequently used to create an innovative fabrication approach based on the generation of stacked structures of NAA-BPFs produced with different PSPA periods. The resulting NAA-BPFs feature characteristic transmission bands, the number, position and width of which across the UV-visible-NIR spectrum can be engineered with precision to create a set of unique bandpass filters. As a proof-of-concept, for the first time, we demonstrate the realisation of NAA-BPFs with two, three and four transmission bandpass windows. Finally, we demonstrate that our approach can also be readily used to broaden the bandwidth of NAA-BPFs by creating stacked NAA-BPFs with slight modifications of the anodisation period. The resulting NAA-BPFs feature transmission bands of unprecedented width, which can be tuned across the UV-visible-NIR spectrum by this anodisation approach.

Experimental

Materials

Aluminium substrates of high purity (99.9997%) and 0.32 mm thickness were acquired from Goodfellow Cambridge Ltd. (UK). Perchloric acid ($HClO_4$), hydrochloric acid (HCl), copper(II) chloride ($CuCl_2$), sulphuric acid (H_2SO_4), phosphoric acid (H_3PO_4) and ethanol (EtOH – C_2H_5OH) were provided by Sigma-Aldrich (Australia) and used as received. Ultrapure water (18.2 MΩ·cm) Option Q–Purelabs (Australia) was used for preparing the solutions used in this study.

Fabrication of NAA-BPFs by pseudo-stepwise pulse anodisation

In this study, a pseudo-stepwise pulse anodisation (PSPA) approach under current density control conditions was used to produce NAA-BPFs. Prior to anodisation, Al square chips (2.25 cm^2) were washed in ethanol and water under sonication for 15 min each, dried under air stream and polished electrochemically in a mixture EtOH:$HClO_4$ 4:1 (*v*:*v*) at 20 V and 5^{0}C for 3 min. The anodisation process was performed in an electrochemical reactor equipped with temperature controller, where the electropolished aluminium chips were exposed to the electrolyte solution through a circular window 1.2 cm in diameter and platinum wire acted as cathode. Al chips were anodised by PSPA in an aqueous solution 1.1 M H_2SO_4, the temperature of which was kept constant at -1^{0}C throughout the anodisation process. The electrolyte solution was modified with 25 *v*% EtOH in order to prevent it from freezing at temperatures below 0^{0}C.[52-53] The anodisation process, described in **Fig. 1a** started with a constant current density step performed at 1.12 mA cm^{-2} for 1 h. During this step, a thin layer of oxide with straight cylindrical nanopores was created and a homogeneous growth rate of the nanopores was achieved. Then, the anodisation process was set to PSPA mode, in the course of which the anodisation current density was pulsed between maximum (J_{max} = 1.12 mA cm^{-2}) and minimum (J_{min} = 0.28 mA cm^{-2}) values in a pseudo-stepwise fashion. Note that the current density pulses in PSPA are asymmetric, where the current density is modified from J_{min} to J_{max} in a stepwise fashion and a linear decrement from J_{max} to J_{min} following a current density ramp (S_{down}) is applied. So, the anodisation period (T_P) (i.e. time between consecutive pulses) is given by **Eq. 1**.

$$T_P = t_{max} + t_{min} + \frac{J_{max} - J_{min}}{S_{down}} \quad (1)$$

where J_{max} and J_{min} are the current density maximum and minimum, respectively, t_{max} and t_{min} are the time lengths at J_{max} and J_{min}, respectively, and S_{down} is the current density ramp from J_{max} to J_{min} (**Fig. 1a**). In this study, t_{max} and t_{min} were set as so $t_{min} = 4t_{max}$, S_{down} was fixed to 0.03061 mA cm^{-2} s^{-1} and the PSPA time was set to 24 h.

The anodisation profiles used in this study to produce NAA-BPFs were created by a custom-designed Labview®-based software. After the anodisation process, the nanoporous structure of NAA-BPFs was widened by wet chemical etching in an aqueous solution 5 *wt*% H_3PO_4 at 35°C.

Engineering and optical tuning of the photonic stop band of NAA-BPFs by the anodisation period (T_P)

As mentioned above, PSPA under the conditions used in our study makes it possible to engineer the effective medium of NAA in depth in order to produce NAA-BPFs (**Figs. 1b and c**). The anodisation period (T_P) was systematically modified from 500 to 1200 s with a step size (ΔT_P) of 100 s in order to assess the effect of this parameter over the optical properties of NAA-BPFs (i.e. positon and width of transmission band and interferometric colours) (**Fig. 1d**). This analysis is critical to achieve a rational understanding of these photonic structures and engineer NAA-BPFs with unique optical properties.

Realisation of NAA-BPFs with selectively positioned transmission bands across the UV-visible-NIR spectrum

To demonstrate the versatility of PSPA for engineering the photonic stop band of NAA and produce optical bandpass filters with unique optical properties, we fabricated stacked NAA-BPFs produced with different anodisation periods. This approach aimed at engineering and positioning the transmission bands of NAA-BPFs across the UV-visible-NIR spectrum in a selective manner. In this experiment, first, we fabricated a set of bi-NAA-BPFs produced with $T_{P\text{-}Top}$ = 500 s and $T_{P\text{-}Bottom}$ = 700 s, $T_{P\text{-}Top}$ = 500 s and $T_{P\text{-}Bottom}$ = 900 s and $T_{P\text{-}Top}$ = 500 s and

$T_{P\text{-}Bottom}$ = 1100 s. These NAA-BPFs were denoted as NAA-BPF$_{500\text{-}700}$, NAA-BPF$_{500\text{-}900}$ and NAA-BPF$_{500\text{-}1100}$, respectively. To further demonstrate the capability of this approach, we fabricated tri- and tetra-NAA-BPFs featuring three and four stacked NAA-BPFs produced with anodisation periods 700, 900 and 1100 s and 500, 700, 900 and 1100 s, respectively (NAA-BPF$_{700\text{-}900\text{-}1100}$ and NAA-BPF$_{500\text{-}700\text{-}900\text{-}1100}$). It is worthwhile stressing that the total anodisation time of the PSPA stage was fixed to 24 h in all the cases and the anodisation time for each NAA-BPF in bi-, tri- and tetra-NAA-BPFs was fixed to 12, 8 and 6 h, respectively.

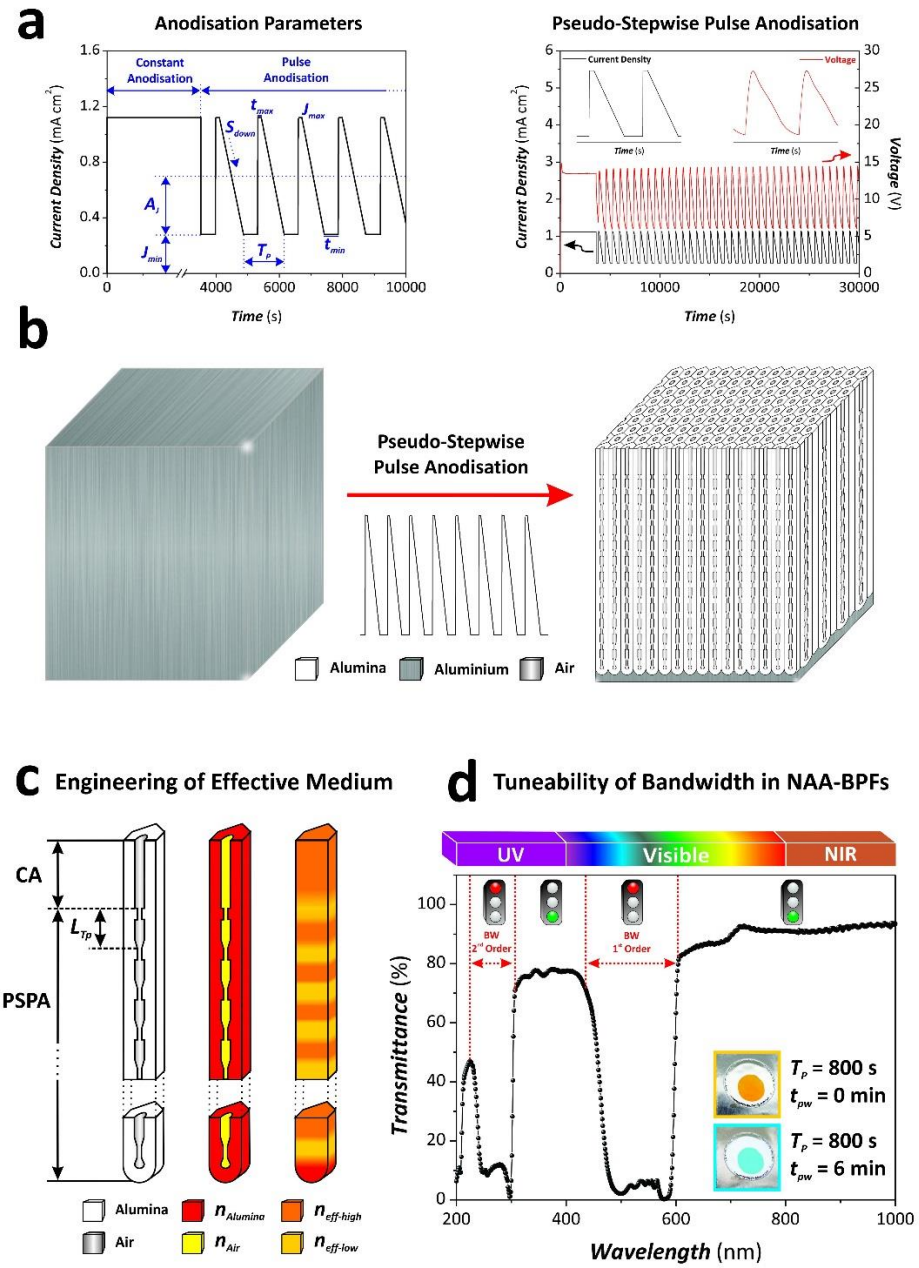

Fig. 1 Conceptual description of pseudo-stepwise pulse anodisation approach used in this study to produce nanoporous anodic alumina optical bandpass filters. a) Example of pseudo-stepwise pulse anodisation profile used to produce NAA-BPFs (left – graphical description of the anodisation parameters defining a pseudo-stepwise pulse anodisation profile: T_P = anodisation period, A_J = anodisation amplitude, J_{min} = minimum of current density, J_{max} = maximum of current density, t_{min} = time at J_{min}, t_{max} = time at J_{max}, S_{down} = current density ramp from J_{max} to J_{min}; left – example of real anodisation profile with insets showing magnified views of current density and voltage for a NAA-BPF produced with T_P = 800 s). b) Scheme showing the conversion of aluminium chips into NAA-BPFs by pseudo-stepwise pulse anodisation. c) Illustration describing the correlation between pore geometry, distribution of individual refractive indexes (i.e. $n_{alumina}$ and n_{air}) and effective medium approximation between low ($n_{eff\text{-}low}$) and high ($n_{eff\text{-}high}$) effective refractive indexes in NAA-BPFs. d) Example of reflection spectrum of a reference NAA-BPF (i.e. T_P = 800 s, A_J = 0.420 mA cm^{-2}, J_{min} = 0.28 mA cm^{-2}, J_{max} = 1.12 mA cm^{-2}, t_{min} = 80.75 s, t_{max} = 323.02 s, N_P = 150 pulses, S_{down} = 0.03061 mA cm^{-2} s^{-1} and t_{pw} = 6 min) showing the characteristic transmission bands and the bandwidth (BW) (1st and 2nd order) across the UV-visible-NIR spectrum with allowed (green) and forbidden (red) pass of light denoted by traffic lights and the characteristic interferometric colour of the representative NAA-BPFs at different pore widening times (i.e. 0 and 6 min).

Optical engineering of the bandwidth of NAA-BPFs by PSPA

To demonstrate how the bandwidth of the transmission window of NAA-BPFs can be precisely engineered by PSPA, we created a set of NAA-BPFs composed of multiple stacked NAA-BPFs featuring small variations of the anodisation period. This approach consists of tuning the bandwidth of the transmission band of NAA-BPFs by changing the number and anodisation periods of stacked NAA-BPFs. Four types of NAA-BPFs were fabricated in this study: namely; i) three-stack NAA-BPF composed of three stacked NAA-BPFs produced with T_P = 700, 725 and 750 s (NAA-BPF$_{3\text{-Stack}}$), ii) five-stack NAA-BPF composed of five stacked NAA-BPFs produced with T_P = 700, 725, 750, 775 and 800 s (NAA-BPF$_{5\text{-Stack}}$), iii) eight-stack NAA-BPF composed of eight stacked NAA-BPFs produced with T_P = 700, 725, 750, 775, 800, 825, 850 and 875 s (NAA-BPF$_{8\text{-Stack}}$) and iv) ten-stack NAA-BPF composed of ten stacked NAA-BPFs produced with T_P = 700, 725, 750, 775, 800, 825, 850, 875, 900 and 925 s (NAA-BPF$_{10\text{-Stack}}$). Note that the total anodisation time of the PSPA stage was fixed to 24 h and the anodisation time for each stack was proportional to the number of stacks in the structure of the resulting NAA-BPFs (i.e. 8, 4.8, 3 and 2.4 h for NAA-BPF$_{3\text{-Stack}}$, NAA-BPF$_{5\text{-Stack}}$, NAA-BPF$_{8\text{-Stack}}$ and NAA-BPF$_{10\text{-Stack}}$, respectively).

Optical characterisation

The transmission spectra of the different NAA-BPFs across the UV-visible-NIR spectrum (i.e. from 200 to 1000 nm) were acquired at normal incidence (i.e. $\theta = 0°$) with a resolution of 1 nm using a UV-visible-NIR spectrometer (Cary 60, Agilent, USA). The interferometric colours displayed by the different NAA-BPFs were characterised by digital images acquired by a Sony HX90V Compact Camera with 18.2 MP and 30x optical zoom and autofocus function under natural illumination, using a black card as background. To record the transmission spectrum of NAA-BPFs, the remaining aluminium substrate was chemically dissolved by wet etching in a saturated solution of HCl/$CuCl_2$ through an etching mask with a circular window 5 mm in diameter.

Structural characterisation

The morphology and structure of NAA-BPFs were analysed by field emission gun scanning electron microscopy (FEG-SEM FEI Quanta 450). The geometric features of NAA-BPFs were established from FEG-SEM images processed by ImageJ (public domain program developed at the RSB of the NIH).[54]

Results and discussion

Morphological and structural characterisation of NAA-BPFs

As shown in **Figs. 1b and c**, the structure of NAA-BPFs can be described as a stack of nanoporous layers of NAA featuring increments and decrements of porosity in depth following a pseudo-stepwise fashion. **Fig. 2** shows a set of representative SEM images of the actual structure of NAA-BPFs produced by PSPA. A top SEM image of these photonic structures reveals a non-organised arrangement of nanopores, which are homogeneously distributed across the surface of the NAA-BPFs (**Fig. 2a**). Note that the anodisation conditions used in this study are not within the self-organisation regimes for NAA. However, these conditions make it possible to produce NAA with higher levels of porosity and to achieve a precise control over this parameter in depth by means of the PSPA profile, which in turn is critical to create photonic structures with precisely engineered optical properties. Cross-sectional view SEM images (**Figs. 2b and c**) show that NAA-BPFs are composed of stacked layers of NAA, the porosity of which is modified in depth in a pseudo-stepwise manner. A magnified cross-sectional view of these photonic structures denotes that the different pseudo-stepwise pulses can be discerned in the structure of NAA-BPFs by physical interfaces between consecutive layers, as indicated by the white arrowheads shown in **Fig. 2c**. The length of each layer within that stacked nanoporous structure (**Fig. 2d**) is defined as the period length (L_{Tp}) (see **Fig. 1c** for a graphical definition) and it was found to follow a linear dependence with the anodisation period (*vide infra*).

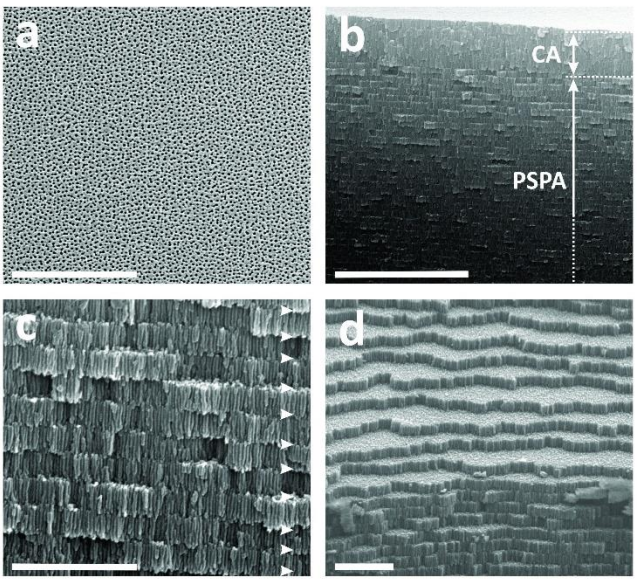

Fig. 2 Representative SEM images of NAA-BPFs produced by pseudo-stepwise pulse anodisation approach. a) General top view SEM image of a NAA-BPF produced with T_P = 900 s, A_J = 0.420 mA cm^{-2}, J_{min} = 0.28 mA cm^{-2}, J_{max} = 1.12 mA cm^{-2}, t_{min} = 100.75 s, t_{max} = 403.02 s, N_P = 150 pulses, S_{down} = 0.03061 mA cm^{-2} s^{-1} and t_{pw} = 6 min) (scale bar = 1 μm). b) General cross-sectional view SEM image of a representative NAA-BPF, where CA and PSPA indicate the NAA layers produced at constant and pseudo-stepwise pulse anodisation modes, respectively (scale bar = 5 μm). c) Magnified view of (a), where white arrowheads denote the physical interfaces between consecutive anodisation pulses - L_{Tp} (scale bar = 1 μm). d) SEM image showing the stacked structure of NAA-BPFs produced by PSPA approach (scale bar = 1 μm).

Effect of the anodisation period on the optical properties of NAA-BPFs

Fig. 3 shows representative anodisation profiles (**Figs. 3a-c**), transmission spectra (**Figs. 3d-f**) and cross-sectional SEM images (**Figs. 3g-i**) of NAA-BPFs produced with T_P = 500, 800 and 1100 s. **Figs. 3d-f** demonstrate that the position of the transmission bands of NAA-BPFs can be precisely tuned across the UV-visible-NIR spectrum by the anodisation period and the pore widening time (see **Fig. S1 ESI**). SEM image analysis revealed that the period length (L_{Tp}) varies linearly with the anodisation period (T_P) with a dependence of 0.243 ± 0.011 nm s^{-1} (**Fig. 3j**). **Fig. 4** summarises the analysis on the position and full width at half maximum (FWHM) of the transmission band of NAA-BPFs produced by PSPA, the anodisation period of

which was varied from 500 to 1200 s with ΔT_P = 100 s. As **Fig. 4a** reveals, the position of the transmission band (λ_{Band}) depends linearly on T_P at any pore widening time (t_{pw}), with a dependence of 0.589 ± 0.012, 0.604 ± 0.015, 0.608 ± 0.015 and 0.576 ± 0.017 nm s^{-1} at 0, 2, 4 and 6 min of pore widening treatment, respectively. It was also observed that the transmittance of the allowed band pass is lower in the UV region of the light spectrum. This phenomenon is associated with the reflection of light by the bulk structure of the NAA-BPF given that NAA presents a strong intrinsic reflection in the UV part of the spectrum. As a result, NAA-BPFs with bands near that region display low allowed band pass (see **Figs. 3d-f**).

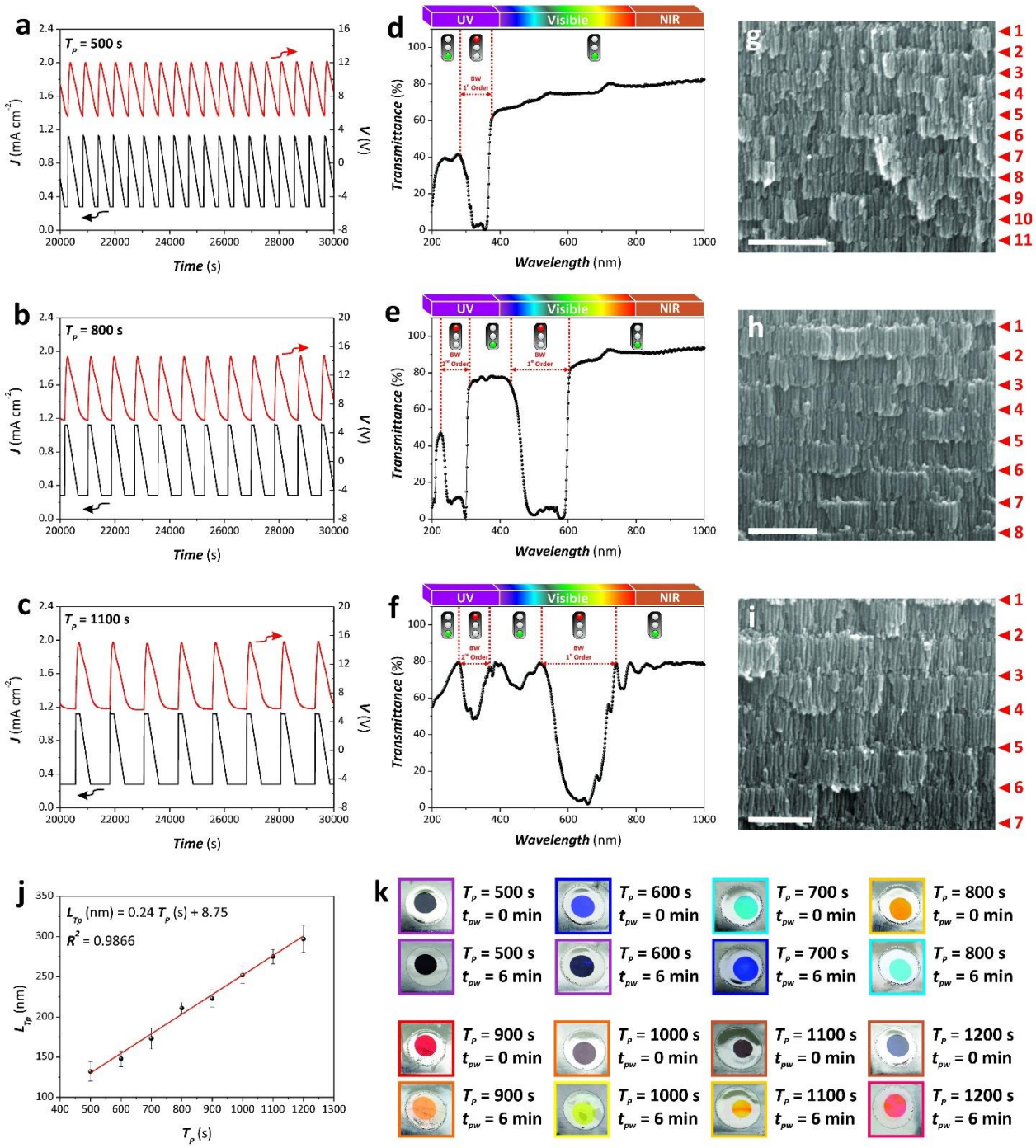

Fig. 3 Tuneability of the characteristic transmission bands of NAA-BPFs by the anodisation period (T_P). a-c) Representative PSPA profiles used to produce NAA-BPFs with T_P = 500 (a), 800 (b) and 1100 s (c) (Note: the rest of parameters was fixed at A_J = 0.420 mA cm^{-2}, J_{min} = 0.28 mA cm^{-2}, J_{max} = 1.12 mA cm^{-2}, N_P = 150 pulses, S_{down} = 0.03061 mA cm^{-2} s^{-1} and t_{pw} = 6 min). d-f) Transmission spectra of NAA-BPFs produced with T_P = 500 (d), 800 (e) and 1100 s (f), where the traffic lights denote allowed (green) and forbidden (red) pass of light (Note: these spectra correspond to t_{pw} = 6 min). g-i) Representative cross-sectional view SEM images of NAA-BPFs produced with T_P = 500, 800 and 1100 s (scale bars = 500 nm) (Note: red arrowheads denote the physical interfaces between anodisation periods - L_{Tp}). j) Linear dependence between the L_{Tp} and T_P. k) Digital pictures revealing the interferometric colours displayed by NAA-BPFs before (t_{pw} = 0 min) and after (t_{pw} = 6 min) pore widening treatment as a function of the anodisation period (Note: the underlying aluminium substrate was chemically removed through an etching mask using a saturated solution of HCl / $CuCl_2$ – diameter of etching mask = 5 mm).

These results confirm that the longer the anodisation period the longer the wavelength at which the characteristic transmission band of NAA-BPFs is located (i.e. red shift) (**Fig. 4a**). Furthermore, it is worthwhile noting that this phenomenon is also reflected in the interferometric colour displayed by these photonic structures, which can be precisely tuned across the UV-visible-NIR spectrum by a combination of the anodisation period and the pore widening time (see **Fig. 3k**).

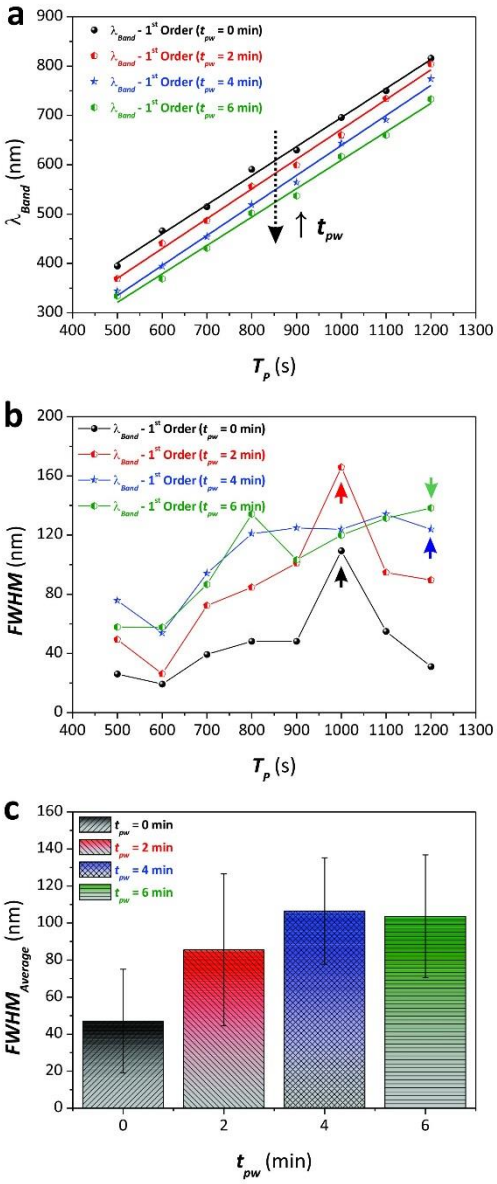

Fig. 4 Effect of the anodisation period (T_P) on the positon (λ_{Band}) and full width at half maximum (FWHM) of the characteristic transmission bands of NAA-BPFs produced by PSPA. a) Linear dependence of λ_{Band} with T_P for NAA-BPFs produced with T_P ranging from 500 to 1200 s with ΔT_P = 100 s at different pore widening times (t_{pw} = 0, 2, 4 and 6 min). b) FWHM of the characteristic transmission bands for the different NAA-BPFs produced in this study at t_{pw} = 0, 2, 4 and 6 min with arrows indicating the maximum FWHM. c) Bar chart showing the average FWHM of these NAA-BPFs as a function of the pore widening time.

Those NAA-BPFs with transmission bands located within the visible range feature vivid colours (from blue to red). In contrast, those NAA-BPFs with the transmission band positioned in the UV or NIR ranges are transparent. **Fig. 4b** shows the FWHM of the characteristic transmission band of NAA-BPFs as a function of the anodisation period. This analysis revealed that, at t_{pw} = 0 and 2 min and t_{pw} = 4 and 6 min the maximum FWHM values are presented by those NAA-BPFs produced with anodisation periods of 1000 and 1200 s, respectively (see arrows shown in **Fig. 4b**). The average FWHM value for all the anodisation periods was found to increase with the pore widening time up to 4 min (**Fig. 4c**), with averages of 47 ± 28, 85 ± 41, 106 ± 29 and 104 ± 33 nm for t_{pw} = 0, 2, 4 and 6 min, respectively.

Fabrication of NAA-BPFs with selectively positioned transmission bands across the UV-visible-NIR spectrum

PSPA is a versatile nanofabrication approach that can be readily used to engineer the photonic stop band of NAA-BPFs in order to create photonic structures with precisely designed optical properties for different applications. In this study, we used a modified PSPA in order to produce stacked NAA-BPFs featuring different anodisation periods. This approach aims to create different transmission windows across the UV-visible-NIR spectrum of NAA-BPFs, the position and number of which can be engineered in a selective manner following this rationale. First, we fabricated a set of bi-NAA-BPFs produced with $T_{P\text{-}Top}$ = 500 s and $T_{P\text{-}Bottom}$ = 700 s, $T_{P\text{-}Top}$ = 500 s and $T_{P\text{-}Bottom}$ = 900 s and $T_{P\text{-}Top}$ = 500 s and $T_{P\text{-}Bottom}$ = 1100 s, denoted as NAA-BPF$_{500\text{-}700}$, NAA-BPF$_{500\text{-}900}$ and NAA-BPF$_{500\text{-}1100}$, respectively (**Fig. 5**).

The structure of bi-NAA-BPFs is composed of two NAA-BPFs (i.e. top and bottom), which are fabricated with different anodisation periods ($T_{P\text{-}Top}$ and $T_{P\text{-}Bottom}$) (**Figs. 5a and b**). **Figs. 5c-e** display representative anodisation profiles and transmission spectra of bi-NAA-BPFs. These photonic structures feature two characteristic transmission bands located at different sections of the UV-visible-NIR spectrum, the position of which is established by the anodisation period of each NAA-BPFs composing the structure of the bi-NAA-BPFs (i.e. top NAA-BPF and bottom NAA-BPF) (**Figs. 5f-h**). For example, the position of the bands corresponding to the different NAA-BPFs composing the structure of bi-NAA-BPFs were located at 295 ± 1 and 422 ± 1 nm for NAA-BPF$_{500\text{-}700}$, 292 ± 1 and 535 ± 1 nm for NAA-BPF$_{500\text{-}900}$ and 342 ± 1 and 698 ± 1 nm for NAA-BPF$_{500\text{-}1100}$, respectively. It was observed that the position of the band corresponding to T_P = 500 s was slightly blue-shifted for NAA-BPF$_{500\text{-}700}$ and NAA-BPF$_{500\text{-}900}$, as compared to that of a mono-NAA-BPF produced with T_P = 500 s (i.e. 395 ± 1 nm, as indicated in **Fig. 4a**). This result occurred for all the bands (i.e. 500, 700, 900 and 1100 s) and it is in good agreement with previously reported studies, where it was found that a decrement of the number of anodisation pulses (i.e. the thickness of the individual NAA-BPFs forming the structure of bi-NAA-BPFs) results in a slight blue shift of the position of the characteristic transmission bands of NAA-BPFs.[55] As commented before (*vide supra*), each NAA-BPF in the structure of bi-NAA-BPFs was produced with an anodisation time of 12 h. It is worthwhile mentioning that the blue shift observed in the 500 s band for the NAA-BPF$_{500\text{-}1100}$ (i.e. from 395 ± 1 nm to 342 ± 1 nm) was less marked than that of NAA-BPF$_{500\text{-}700}$ and NAA-BPF$_{500\text{-}900}$ due to the merger of the first order band of 500 s and the second order band of 1100 s. **Table S1 (ESI)** summarises the obtained results for all the bands in bi-NAA-BPFs. Another interesting phenomenon observed in bi-NAA-BPFs is that the interferometric colour

featured by these photonic structures is established by the band located at longer wavelengths. So, NAA-BPF$_{500\text{-}700}$, NAA-BPF$_{500\text{-}900}$ and NAA-BPF$_{500\text{-}1100}$ were found to display transparent (UV), cyan and red interferometric colour, respectively. Digital pictures shown in **Figs. 5f-h** reveal the interferometric colours of these NAA-BPFs at different etching times (from 0 to 6 min).

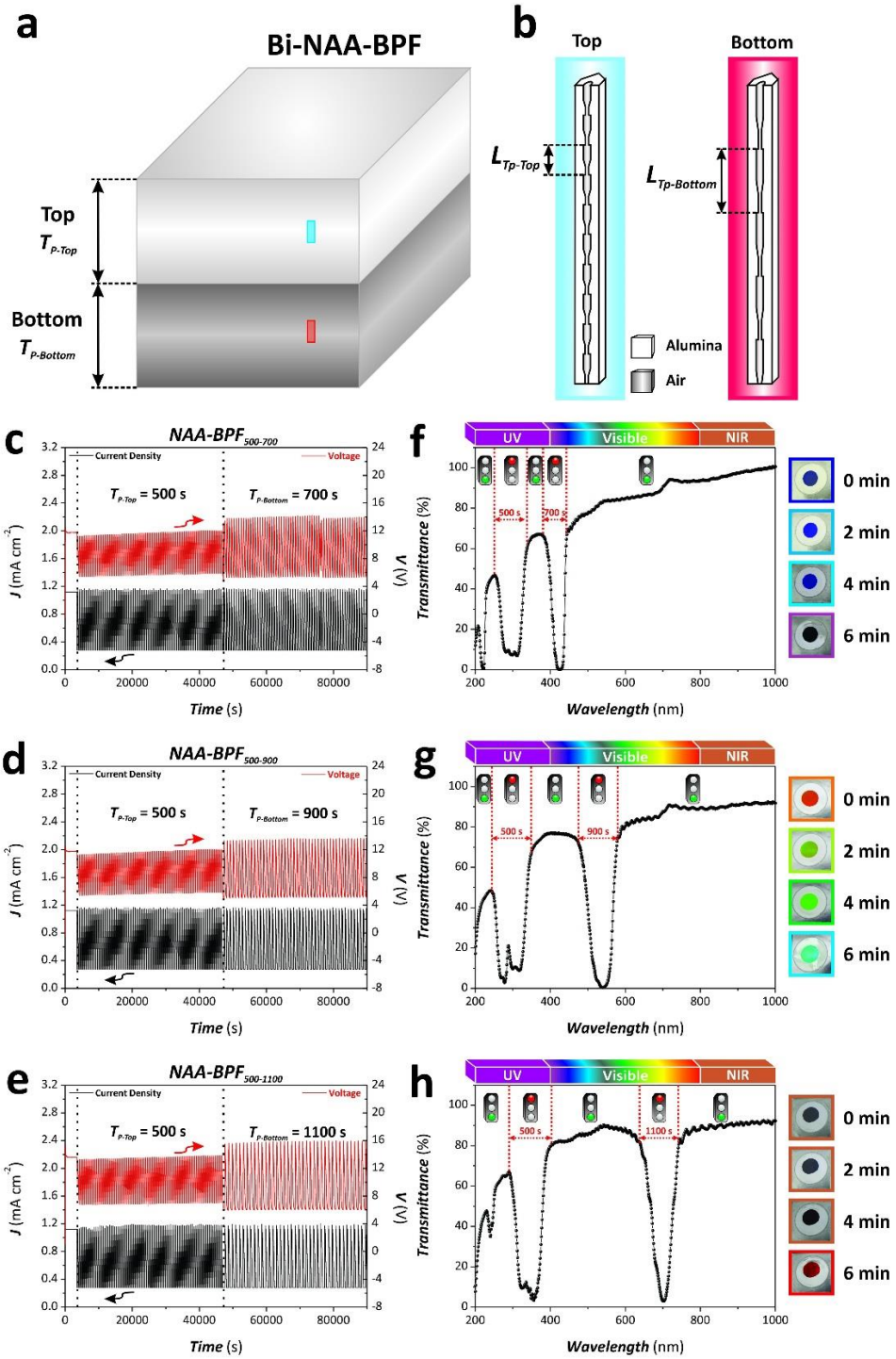

Fig. 5 Fabrication and optical characterisation of bi-NAA-BPFs produced by pseudo-stepwise pulse anodisation. a) Schematic diagram showing the general structure of bi-NAA-BPFs. b) Illustration showing details of the nanoporous structure of bi-NAA-BPFs with top and bottom layers fabricated with different anodisation periods ($T_{P\text{-}Top} < T_{P\text{-}Bottom} \rightarrow L_{Tp\text{-}Top} < L_{Tp\text{-}Bottom}$). c-e) Representative anodisation profiles used to produce bi-NAA-BPFs (c – NAA-BPF$_{500\text{-}700}$, d – NAA-BPF$_{500\text{-}900}$ and e – NAA-BPF$_{500\text{-}1100}$). f-h) Transmission spectra of bi-NAA-BPFs produced with top and bottom layers of different anodisation period (f – NAA-BPF$_{500\text{-}700}$, g – NAA-BPF$_{500\text{-}900}$ and h – NAA-BPF$_{500\text{-}1100}$), where the traffic lights denote allowed (green) and forbidden (red) pass of light, and insets showing the characteristic interferometric colours displayed by these NAA-BPFs at different pore widening times (Note: these spectra correspond to t_{pw} = 6 min).

To further demonstrate the versatility of this approach, we fabricated a set of tri- and tetra-NAA-BPFs featuring three and four stacked NAA-BPFs produced with anodisation periods 700, 900 and 1100 s and 500, 700, 900 and 1100 s, respectively (i.e. NAA-BPF$_{700\text{-}900\text{-}1100}$ and NAA-BPF$_{500\text{-}700\text{-}900\text{-}1100}$) (**Fig. 6**). The total anodisation time of the PSPA stage was fixed to 24 h in all the cases and the anodisation time for each NAA-BPF forming the structure of tri- and tetra-NAA-BPFs was fixed to 8 and 6 h, respectively (**Figs. 6a and b**). **Figs. 6c and d** show representative anodisation profiles of the tri- and tetra-NAA-BPFs fabricated in this study and **Figs. 6e and f** display the transmission spectra of these complex NAA-BPFs produced by PSPA. As these spectra indicate, these NAA-BPFs feature three and four characteristic transmission bands, the position of which across the UV-visible-NIR spectrum is established by the anodisation period of each stack composing the structure of the tri- and tetra-NAA-BPFs. Likewise in the case of bi-NAA-BPFs, the position of these bands is slightly blue-shifted due to the decreasing number of anodisation pulses. For instance, the position of the bands corresponding to the NAA-BPFs produced with T_P = 700, 900 and 1100 s for NAA-BPF$_{700\text{-}900\text{-}1100}$ are located at 439 ± 1, 589 ± 1 and 722 ± 1 nm, respectively, which are slightly blue-shifted as compared to the position of these bands in mono-NAA-BPFs (see **Fig. 4a**). This phenomenon was also observed in the case of NAA-BPF$_{500\text{-}700\text{-}900\text{-}1100}$, the bands of which were located at 331 ± 1 nm (500 s), 447 ± 1 nm (700 s), 583 ± 1 nm (900 s) and 741 ± 1 nm (1100s). A comprehensive summary of these results is compiled in **Table S1 (ESI)**. In contrast to bi-NAA-BPFs, we observed that the interferometric colour of tri- and tetra-NAA-BPFs features a complex patter. Prior to pore widening treatment, tri- and tetra-NAA-BPFs feature transparent colour as the position of the band produced with the longest anodisation period (i.e. T_P = 1100 s) is located in the NIR range. However, the positon of the transmission bands of tri- and tetra-NAA-BPFs undergoes a blue shift with the pore widening treatment from 0 to 6 min, as denoted by the digital pictures shown in **Figs. 6e and f**. As a result of this treatment, these NAA-BPFs feature iridescent colours, with a complex mixture of green and purple.

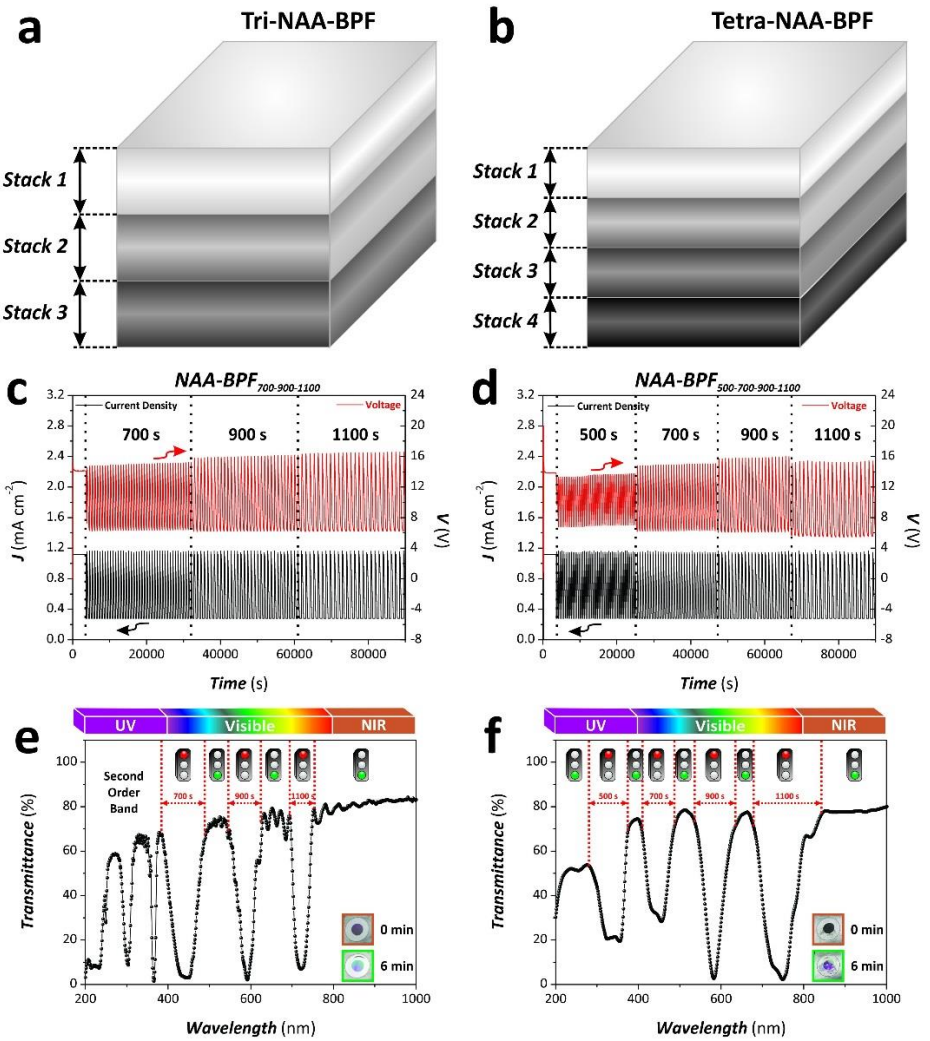

Fig. 6 Fabrication and optical characterisation of tri- and tetra-NAA-BPFs produced by pseudo-stepwise pulse anodisation. a-b) Schematic diagram illustrating the general structure of tri- and tetra-NAA-BPFs (a – NAA-BPF$_{700\text{-}900\text{-}1100}$ and b – NAA-BPF$_{500\text{-}700\text{-}900\text{-}1100}$). c-d) Representative anodisation profiles used to produce tri- and tetra-NAA-BPFs (c – NAA-BPF$_{700\text{-}900\text{-}1100}$ and d – NAA-BPF$_{500\text{-}700\text{-}900\text{-}1100}$). e-f) Transmission spectra of tri- and tetra-NAA-BPFs produced with stacked NAA-BPFs of different anodisation period (e – NAA-BPF$_{700\text{-}900\text{-}1100}$ and f – NAA-BPF$_{500\text{-}700\text{-}900\text{-}1100}$), where the traffic lights denote allowed (green) and forbidden (red) pass of light, and insets showing the characteristic interferometric colours displayed by NAA-BPFs at different pore widening times (Note: these spectra correspond to t_{pw} = 6 min).

Engineering of the bandwidth of NAA-BPFs by pseudo-stepwise pulse anodisation

The rationale generated from the experiments described above encouraged us to design an anodisation strategy aiming at engineering the width of the transmission band of NAA-BPFs by PSPA. To this end, we fabricated a set of NAA-BPFs composed of multiple stacked NAA-BPFs featuring small variations of the anodisation period (i.e. ΔT_P = 25 s), the conditions of which were established by a series of preliminary experiments. This approach makes it achievable to tune the bandwidth of the transmission band of NAA-BPFs by changing the number of stacked NAA-BPFs and the anodisation period of each NAA-BPF. As a proof-of-concept, four types of NAA-BPFs featuring different bandwidths were fabricated: namely; i) three-stack NAA-BPF composed of three stacked NAA-BPFs produced with T_P = 700, 725 and 750 s (NAA-BPF$_{3\text{-Stack}}$), ii) five-stack NAA-BPF composed of five stacked NAA-BPFs produced with T_P = 700, 725, 750, 775 and 800 s (NAA-BPF$_{5\text{-Stack}}$), iii) eight-stack NAA-BPF composed of eight stacked NAA-BPFs produced with T_P = 700, 725, 750, 775, 800, 825, 850 and 875 s (NAA-BPF$_{8\text{-Stack}}$) and iv) ten-stack NAA-BPF composed of ten stacked NAA-BPFs produced with T_P = 700, 725, 750, 775, 800, 825, 850, 875, 900 and 925 s (NAA-BPF$_{10\text{-Stack}}$). **Fig. 7** shows the anodisation profiles and transmission spectra of NAA-BPF$_{3\text{-Stack}}$, NAA-BPF$_{5\text{-Stack}}$, NAA-BPF$_{8\text{-Stack}}$ and NAA-BPF$_{10\text{-Stack}}$. Likewise in the case of bi-, tri- and tetra-NAA-BPFs, the total anodisation time of the PSPA stage was fixed to 24 h and the anodisation time for each stack was proportional to the number of stacks composing the structure of these NAA-BPFs. So, each stacked NAA-BPF composing the structure of NAA-BPF$_{3\text{-Stack}}$, NAA-BPF$_{5\text{-Stack}}$, NAA-BPF$_{8\text{-Stack}}$ and NAA-BPF$_{10\text{-Stack}}$ were produced with 8, 4.8, 3 and 2.4 h, respectively. As the anodisation profiles for NAA-BPF$_{3\text{-Stack}}$, NAA-BPF$_{5\text{-Stack}}$, NAA-BPF$_{8\text{-Stack}}$ and NAA-BPF$_{10\text{-Stack}}$ show, the approach used in our study to engineer the nanoporous structure of NAA in depth can be performed in a continuous fashion by PSPA, with a progressive stepwise increment of the anodisation period at steps of 25 s (**Figs. 7a-d**). **Figs. 7e-h** show representative transmission spectra of NAA-BPF$_{3\text{-Stack}}$, NAA-BPF$_{5\text{-Stack}}$, NAA-BPF$_{8\text{-Stack}}$ and NAA-BPF$_{10\text{-Stack}}$, which display a characteristic transmission band, the width of which is established by the number of stacked NAA-BPFs composing the structure of these complex photonic crystal structures. It was verified that the position of the transmission band of NAA-BPF$_{3\text{-Stack}}$, NAA-BPF$_{5\text{-Stack}}$, NAA-BPF$_{8\text{-Stack}}$ and NAA-BPF$_{10\text{-Stack}}$ is located at 448 ± 1, 485 ± 1, 489 ± 1 and 503 ± 3 nm, respectively. This analysis reveals that this anodisation approach makes it possible to keep the central positon of the transmission band, while only incurring a slight red shift. Furthermore, as **Figs. 7e-h** show, the FWHM of these bands increases with the number of stacked NAA-BPFs (i.e. 111 ± 1, 151 ± 1, 192 ± 1 and 325 ± 2 nm, for NAA-BPF$_{3\text{-Stack}}$, NAA-BPF$_{5\text{-Stack}}$, NAA-BPF$_{8\text{-Stack}}$ and NAA-BPF$_{10\text{-Stack}}$, respectively). These results demonstrate that this anodisation strategy can be readily used to crease optical bandpass filters with tuneable band width. In addition, we also observed that the interferometric colour displayed by NAA-BPF$_{3\text{-Stack}}$, NAA-BPF$_{5\text{-Stack}}$, NAA-BPF$_{8\text{-Stack}}$ and NAA-BPF$_{10\text{-Stack}}$ is red-shifted with the increasing number of stacks of longer anodisation period, as revealed by the digital pictures shown in **Fig. 7**. This is in good agreement with the slight red shift observed in the central position of the transmission band (*vide supra*). A pore widening treatment can also be used to tune the interferometric of these photonic crystal structures across the UV-visible-NIR spectrum.

Conclusions

To summarise, this study is the first realisation of nanoporous anodic alumina optical bandpass filters produced by pseudo-stepwise pulse anodisation. This rationally designed pulse-like anodisation approach makes it possible to engineer the effective medium of NAA in depth in order to create a set of optical bandpass filters with unique advanced optical properties. First, we have established the effect of the anodisation period as the parameter of choice for tuning the position and width of the transmission bands of NAA across the UV-visible-NIR spectrum. A set of NAA-BPFs were produced with different anodisation periods, ranging from 500 to 1200 s with a step size of 100 s. The assessment of the optical properties of these photonic crystal structures revealed that the anodisation period provides a suitable means of controlling both the positon of the characteristic transmission bands and the interferometric colours displayed by NAA-BPFs. Following this rationale, we have demonstrated that combination of stacked NAA-BPFs consisting of stacks of NAA produced with different PSPA periods can be readily used to create a set of unique and highly selective optical bandpass filters with characteristic transmission bands, the position, width and number of which can be engineered with precision across the UV-visible-NIR spectrum. The realisation of bi-, tri- and tetra-NAA-BPFs was successfully demonstrated. To conclude, as a proof-of-concept, we have shown that the superposition of stacked NAA-BPFs produced with slight modifications of the anodisation period enables the fabrication of NAA-BPFs with unprecedented broad transmission bands across the UV-visible-NIR spectrum. This strategy has also been demonstrated an optimal method for tuning the transmission band width of NAA-BPFs.

The results obtained from our study constitute the first comprehensive rationale towards the engineering of advanced NAA-BPFs with fully controllable photonic properties. These unique photonic crystal structures could become a promising alternative to traditional bandpass filters based on glass and plastic due to their cost-competitive and industrially scalable fabrication process and their versatility, opening up new opportunities to develop innovative photonic nanostructures.

PAPER

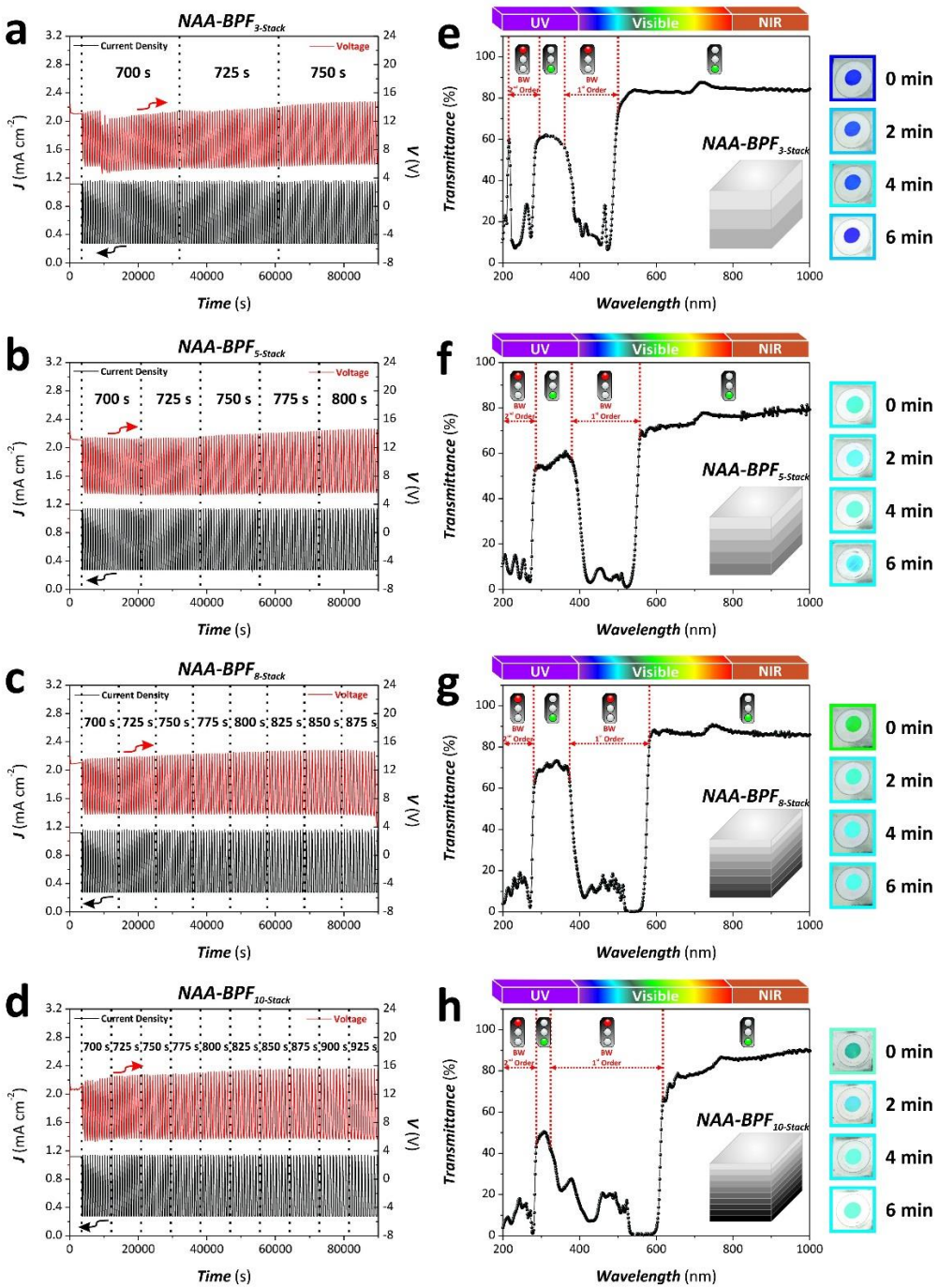

Fig. 7 Engineering of the transmission band width of NAA-BPFs by pseudo-stepwise pulse anodisation. a-d) Representative anodisation profiles of NAA-BPFs featuring bands of different widths (a – NAA-BPF$_{3\text{-Stack}}$, b – NAA-BPF$_{5\text{-Stack}}$, c – NAA-BPF$_{8\text{-Stack}}$ and d – NAA-BPF$_{10\text{-Stack}}$). e-h) Transmission spectra of NAA-BPFs produced with stacked NAA-BPFs of different anodisation period (e – NAA-BPF$_{3\text{-Stack}}$, f – NAA-BPF$_{5\text{-Stack}}$, g – NAA-BPF$_{8\text{-Stack}}$ and h – NAA-BPF$_{10\text{-Stack}}$), where the traffic lights denote allowed (green) and forbidden (red) pass of light, and insets showing the characteristic interferometric colours of NAA-BPFs at different pore widening times with schematic illustrations showing the stacked structure of these photonic crystal structures (Note: these spectra correspond to t_{pw} = 6 min).

Acknowledgements

Authors acknowledge the support provided by the Australian Research Council (ARC) through the grants number DE140100549, DP120101680 and FT110100711 and the School of Chemical Engineering (UoA). Authors also thank the Adelaide Microscopy (AM) centre for FEG-SEM characterisation.

Notes and references

[1]School of Chemical Engineering, The University of Adelaide, Engineering North Building, 5005 Adelaide, Australia.
[2]Institute for Photonics and Advanced Sensing (IPAS), The University of Adelaide, 5005 Adelaide, Australia.
[3]ARC Centre of Excellence for Nanoscale BioPhotonics (CNBP), The University of Adelaide, 5005 Adelaide, Australia.
*E-mails: abel.santos@adelaide.edu.au ; dusan.losic@adelaide.edu.au

Dr. Abel Santos conceived the idea and designed the experimental part of this work. Taj Pereira carried out the experiments assisted by Cheryl Suwen Law and Dr. Abel Santos. The obtained results were discussed and analysed by all the authors. The final version of the manuscript was written through contributions of all the authors. All the authors have given their approval to the final version of the manuscript.

Electronic Supplementary Information (ESI) available: The Supporting Information file contains an example demonstrating the effect of pore widening on the position and width of the transmission band of a NAA-BPF and a comprehensive table summarising the position and FWHM of the different bands of the NAA-BPFs produced in this study. See DOI: 10.1039/b000000x/

1 H. A. Macleod, *Thin-film optical filters*, CRC Press, Taylor & Francis Group, Florida, 2010.
2 B. E. A. Saleh and M. C. Teich, *Fundamentals of photonics*, John Wiley & Sons, Inc., Hoboken, New Jersey, 2007.
3 D. Losic and A. Santos (Eds.), *Nanoporous alumina: Fabrication, structure, properties and applications*, Springer International Publishing, Switzerland, 2015.
4 D. Losic and A. Santos (Eds.), *Electrochemically Engineered Nanoporous Materials: Methods, Properties and Applications*, Springer International Publishing, Switzerland, 2015.
5 M. J. Sailor, *Porous silicon in practice: Preparation, characterization and applications*, WILEY-VCH Verlag GmbH & Co. KGaA, Weinheim, 2012.
6 V. Lehmann, *Electrochemistry of silicon - Instrumentation, science, materials and applications*, WILEY-VCH Verlag GmbH & Co. KGaA, Weinheim, 2002.
7 A. Santos, T. Kumeria and D. Losic, *Materials*, 2014, **7**, 4297-4320.
8 T. Kumeria, A. Santos and D. Losic, *Sensors*, 2014, **14**, 11878-11918.
9 J. Choi, Y. Luo, R. B. Wehrspohn, R. Hillebrand, J. Schilling and U. Gösele, *J. Appl. Phys.*, 2003, **8**, 4757-4762.
10 H. Masuda, M. Ohya, H. Asoh, M. Nakao, M. Nohtomi, and T. Tamamura, *Jpn. J. Appl. Phys.*, 1999, **38**, L 1403-L 1405.
11 H. Masuda, M. Ohya, K. Nishio, H. Asoh, M. Nakao, M. Nohtomi, A. Yokoo, and T. Tamamura, *Jpn. J. Appl. Phys.*, 2000, **39**, L 1039-L 1041.
12 I. Mikulskas, S. Juodkazis, R. Tomasiunas, and J. G. Dumas, *Adv. Mater.*, 2001, **13**, 1574-1577.
13 H. Masuda, M. Ohya, H. Asoh and K. Nishio, *Jpn. J. Appl. Phys.*, 2001, **40**, L 1217-L 1219.
14 W. Lee, R. Ji, U. Gösele and K. Nielsch, *Nat. Mater.*, 2006, **5**, 741-747.
15 W. Lee and J. S. Park, *Chem. Rev.*, 2014, **114**, 7487-7556.
16 Y. Chen, A. Santos, D. Ho, Y. Wang, T. Kumeria, J. Li, C. Wang and D. Losic, *Electrochim. Acta*, 2015, **174**, 672-681.
17 W. Cheng, M. Steinhart, U. Gösele and R. B. Wehrspohn, *J. Mater. Chem.* 2007, **17**, 3493-3495.
18 H. Masuda and K. Fukuda, *Science*, 1995, **268**, 1466-1468.
19 H. Masuda and F. J. Hasegwa, *Electrochem. Soc.*, 1997, **144**, L127-L130.
20 H. Masuda, K. Yada and A. Osaka, *Jpn. J. Appl. Phys.*, 1998, **37**, L 1340-L 1342.
21 K. Nielsch, J. Choi, K. Schwirn, R. B. Wehspohn and U. Gösele, *Nano Lett.* 2002, **2**, 677-680.
22 K. Schwirn, W. Lee, R. Hillebrand, M. Steinhart, K. Nielsch and U. Gösele, *ACS Nano*, 2008, **2**, 302-310.
23 W. Lee, K. Schwirn, M. Steinhart, E. Pippel, R. Scholz and U. Gösele, *Nat. Nanotechnol.*, 2008, **3**, 234-239.
24 W. Lee, J. C. Kim and U. Gösele, *Adv. Funct. Mater.*, 2009, **19**, 1-7.
25 W. Lee, J. C. Kim, *Nanotechnology*, 2010, **21**, 485304.
26 D. Losic, M. Lillo and D. Losic Jr., *Small*, 2009, **5**, 1392-1397.
27 D. Losic and D. Losic Jr., *Langmuir*, 2009, **25**, 5426-5431.
28 W. Lee, R. Scholz and U. Gösele, *Nano Lett.* 2008, **8**, 2155-2160.
29 A. Santos, L. Vojkuvka, M. Alba, V. S. Balderrama, J. Ferré-Borrull, J. Pallarès and L. F. Marsal, *Phys. Stat. Sol. A*, 2012, **10**, 2045-2048.
30 A. Santos, J. M. Montero-Moreno, J. Bachmann, K. Nielsch, P. Formentín, J. Ferré-Borrull, J. Pallarès and L. F. Marsal, *ACS Appl. Mater. Interfaces*, 2011, **3**, 1925-1932.
31 T. Kumeria, M. M. Rahman, A. Santos, J. Ferré-Borrull, L. F. Marsal and D. Losic, *Anal. Chem.*, 2014, **86**, 1837-1844.
32 T. Kumeria, M. M. Rahman, A. Santos, J. Ferré-Borrull, L. F. Marsal and D. Losic, *ACS Appl. Mater. Interfaces*, 2014, **6**, 12971-12978.

33 T. Kumeria, A. Santos, M. M. Rahman, J. Ferré-Borrull, L. F. Marsal and D. Losic, *ACS Photonics*, 2014, **1**, 1298-1306.

34 A. Santos, T. Kumeria, Y. Wang and D. Losic, *Nanoscale*, 2014, **6**, 9991-9999.

35 A. Santos, V. S. Balderrama, M. Alba, P. Formentín, J. Ferré-Borrull, J. Pallarès and L. F. Marsal, *Adv. Mater.*, 2012, **24**, 1050-1054.

36 Y. Wang, Y. Chen, T. Kumeria, F. Ding, A. Evdokiou, D. Losic and A. Santos, *ACS Appl. Mater. Interfaces*, 2015, **7**, 9879-9888.

37 A. Santos, T. Kumeria and D. Losic, *Anal. Chem.*, 2013, **85**, 7904-7911.

38 G. Macias, L. P. Hernándex-Eguía, J. Ferré-Borrull, J. Pallarès and L. F. Marsal, *ACS Appl. Mater. Interfaces*, 2013, **5**, 8093-8098.

39 Y. Chen, A. Santos, Y. Wang, T. Kumeria, C. Wang, J. Li and D. Losic, *Nanoscale*, 2015, **7**, 7770-7779.

40 A. Santos, T. Kumeria and D. Losic, *TrAC, Trends Anal. Chem.*, 2013, **44**, 25-38.

41 Y. Chen, A. Santos, Y. Wang, T. Kumeria, J. Li, C. Wang and D. Losic, *ACS Appl. Mater. Interfaces*, 2015, **7**, 19816-19824.

42 T. Kumeria, A. Santos and D. Losic, *ACS Appl. Mater. Interfaces*, 2013, **5**, 11783-11790.

43 Y. Chen, A. Santos, Y. Wang, T. Kumeria, J. Li, C. Wang and D. Losic, *ACS Appl. Mater. Interfaces* 2015, **7**, 19816-19824.

44 Y. Chen, A. Santos, Y. Wang, T. Kumeria, D. Ho, J. Li, C. Wang and D. Losic, *Sci. Rep.* 2015, **5**, 12893.

45 T. Kumeria, K. Gulati, A. Santos and D. Losic, *ACS Appl. Mater. Interfaces* 2013, **5**, 5436-5442.

46 A. Santos, M. S. Aw, M. Bariana, T. Kumeria, Y. Wang and D. Losic, *J. Mater. Chem. B*, 2014, **2**, 6157-6182.

47 C. S. Law, A. Santos, T. Kumeria and D. Losic, *ACS Appl. Mater. Interfaces* 2015, **7**, 3846-3853.

48 Y. Wang, G. Kaur, Y. Chen, A. Santos, D. Losic and A. Evdokiou, *ACS Appl. Mater. Interfaces* 2015, **7**, 27140-27151.

49 Y. Wang, G. Kaur, A. Zysk, V. Liapis, S. Hay, A. Santos, D. Losic and A. Evdokiou, *Biomaterials*, 2015, **46**, 117-130.

50 Y. Wang, A. Santos, G. Kaur, A. Evdokiou and D. Losic, *Biomaterials*, 2014, **35**, 5517-5526.

51 A. Santos, C. S. Law, T. Pereira and D. Losic, *Nanoscale*, 2016, **8**, 8091-8100.

52 A. Santos, P. Formentín, J. Ferré-Borrull, J. Pallarès and L. F. Marsal, *Mater. Lett.*, 2012, **67**, 296-299.

53 Y. Wang, A. Santos, A. Evdokiou and D. Losic, *Electrochim. Acta*, 2015, **154**, 379-386.

54 M. D. Abràmoff, P. J. Magalhaes and S. J. Ram, *Biophotonics Int.*, 2004, **11**, 36-42.

55 A. Santos, J. Yoo, C. V. Rohatgi, T. Kumeria, Y. Wang and D. Losic, *Nanoscale* 2016, **8**, 1360-1373.

